Commitment of Fast-Responding Storage Devices to Mimic Inertia for the Enhancement of Primary Frequency Response

Ti Xu, *Student Member, IEEE*, Wonhyeok Jang, *Student Member, IEEE*, and Thomas Overbye, *Fellow, IEEE*

***Abstract*—One distinctive feature of renewable energy resources is that they contribute little inertia to power systems. With less system inertia, power grid is less capable of resisting frequency deviation from its nominal value in the first few seconds after disturbances. However, fast-responding storage devices can mimic inertial responses through some specified control algorithm. Thus, this paper focuses on the economic aspect of resource inertia as a service to the grid operation and aims to find a minimum-cost commitment of fast-acting storage devices for the enhancement of primary frequency responses. Costs are assigned to those storage resources and a commitment cost minimization problem is formulated with nonlinear primary frequency response constraints. A tractable iterative solution approach is developed and a sensitivity-based method through a rapidly solvable linear approximation of the nonlinear constraints is proposed to reduce the computational burdens of solving the optimization problem for large-scale systems. The effectiveness of the proposed methods is demonstrated using simulation results obtained using the 118-bus IEEE reliability test system.**

***Index Terms*—Fast-responding storage, primary frequency response, rapid solvable iterative solution approach, resource inertia, sensitivity-based approximation, transient stability constraints.**

I. Introduction

COMPARED to conventional units, modern renewable resources connected to grids via power electronics have distinctive characteristics, one of which is their low or zero inertia. The increasing utilization of renewable resources causes a significant reduction in the total system inertia, which is directly related to the rate of change of frequency (RoCoF) and the minimum/maximum frequency during the first several seconds after disturbances [1]. Decreasing system inertia increases the probability of violation in post-contingency RoCoF or frequency limits. Such violations may trigger relays for generators or loads, and may sequentially cause equipment damages or cascading failure in extreme cases. Recently, ERCOT proposed synchronous inertial response and fast frequency response services as future ancillary services to deal with integration of non-synchronous generations [2]. NERC also specifies in their reliability standard BAL-003-1 that balancing authorities should have sufficient frequency responses to maintain the interconnection frequency within certain bounds [3].

Associating a value with inertial responses would provide an incentive for newer technologies to incorporate frequency response capabilities. There have been some preliminary works on the system inertial response. In [4] and [5], authors developed a mathematic closed-form expression for power system frequency response using a simplified model without considering the economic aspect of inertia services. Works [6] and [7] constructed a market-based model with constraints on the amount of total system inertia, but there might exist biases on the selection of total inertia value bounds and computational burdens from iteratively solving the market optimization problem for large-scale systems. Thus, this work aims to study the minimum-cost commitment problem of multi-site fast-responding storage devices (FSDs) to mimic inertia for the enhancement of primary frequency responses (PFR). Specifically, this paper focuses on the system frequency response of the first few seconds, after a disturbance, during which resource inertia plays a critical role in maintaining the frequency and, aims to find the minimum-cost commitment of FSDs to offer sufficient virtual inertia.

Two possible approaches to mimic inertial responses after a disturbance could be done by controlling power outputs of FSDs at the generation side or managing interruptible loads at the demand side [8]–[10]. Storage devices have a wide range of applications in power grids. Work [11] summarizes results on utilization of storage to increase transmission capability of congested transmission network. In [12], authors evaluate the benefits of battery storage for energy arbitrage, power balancing service, outage mitigation and so on. Energy storage devices also have the potential to mitigate the impacts of uncertainty introduced by renewable energy sources [13] and to improve power usage efficiency [14]. ABB integrates batteries, power converters, and system control into a single solution that provides highly reliable and accurate frequency regulation at much faster speeds than other technologies [15]. Empirical experience has proven a successful implementation and deployment of several grid-scale energy storage projects for frequency regulation services [16]. Several researchers in [17] also demonstrate the

Manuscript received June 9, 2016; revised December 22, 2016, April 4, 2017, and June 29, 2017; accepted July 25, 2017. Date of publication August 4, 2017; date of current version February 16, 2018. This work was supported by the U.S. Department of Energy Consortium for Electric Reliability Technology Solutions (CERTS). Paper no. TPWRS-00874-2016. *(Corresponding author: Ti Xu.)*

The authors are with the University of Illinois at Urbana-Champaign, Champaign, IL 61820 USA (e-mail: txu20@illinois.edu; wjang7@illinois.edu; overbye@illinois.edu).

Color versions of one or more of the figures in this paper are available online at http://ieeexplore.ieee.org.

Digital Object Identifier 10.1109/TPWRS.2017.2735990

valuable properties of energy storage for frequency regulation on the electric grid.

As discussed in [18], inertial responses from most modern MW-level wind turbines are trivial since they are concocted to power grids via electronic devices. Thus, grid frequency deviations may not cause wind turbines to provide primary frequency responses via inertia. However, it is possible to control wind plants to provide virtual inertial response to some extent. GE's WindINERTIA is developed to deal with under-frequency contingencies by reserving a portion of available wind generation. Due to uncertainty and variability of renewable energy, the capability of renewable energy plants is heavily on weather condition. Therefore, in this paper, we focus on the generation side, specifically on the interplay between the enhanced system primary frequency response and the commitment of FSDs. Costs are associated with committing those FSDs to mimic inertia and minimum-cost optimization problems are formulated to investigate the value of inertia services to the grid operation. Transient stability differential and algebraic equation (DAE) system models are used to specify the frequency constraints. The presented algorithm uses an iterative solution of a mixed-integer linear programing (MILP) problem while ensuring nonlinear DAE-modeled constraints are satisfied. A computationally tractable sensitivity-based benefit measure is proposed for the linearization of the frequency constraints and to reduce the computational burden of the iterative algorithm for large systems. The proposed rapidly-solvable simulation algorithm is able to study which storage parameters and how much they come into play for primary frequency response and how much storage devices and their locations play a role in meeting the constraint. The proposed method in this paper could serve as a tool for system operators to price inertia services.

There are six more sections in this paper. Section II introduces the FSD resources and develops the control algorithm to mimic inertia. Section III presents the minimum-cost FSD commitment problem. An iterative solution algorithm is developed in Section IV and we further improve the performance of the proposed algorithm by introducing sensitivity-based benefit measures in Section V. The usefulness of the solution approach is demonstrated using several simulation results in Section VI. Conclusions and future work are given in Section VII.

II. Virtual Inertia Provision

Inertial response can be mimicked by using FSDs since they can react to its maximum charging/discharging rate within 1 ms [19], [20]. This work focuses on the primary frequency responses that cover up to tens of seconds. Without any specified control strategy, post-contingency storage output p_s in p.u. (P_s in MW) remains at its initial value p_{s0} (P_{s0})[1] within a few seconds after contingency and thus such FSDs make no contribution to the system transient stability. We make use of the fast-responding advantages to design a control algorithm to provide some virtual inertia H_s into the system. The core idea of this design is to control storage output such that local frequency behaves as if there is an additional inertia of value H_s with storage output remaining at its initial value p_{s0} (Base: S_B in MVA). The local frequency is represented by f_i in p.u. with the nominal value $f_B = 60$ Hz. Assuming that there is a virtual rotating speed ω_i in p.u., corresponding to the per-unit frequency f_i, we have $\omega_i = f_i$ with its nominal value $\omega_B = 2\pi f_B$ in rad/s [21]. As such, the control algorithm developed in [9], [10] becomes:

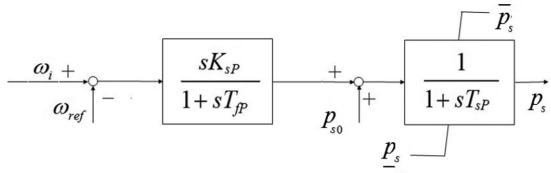

Fig. 1. Simplified structure of the grid-connected storage system.

$$\Delta p_s = p_s - p_{s0} = -2H_s \Delta\dot{\omega}_i = -2H_s\dot{\omega}_i \tag{1a}$$

$$\Delta p_s \in [\underline{p}_s - p_{s0}, \bar{p}_s - p_{s0}] \tag{1b}$$

We observe that the control signal is purely dependent on the local frequency. This can be verified by a more intuitive derivation with the assumption that the FSD has a virtual inertia of $H_s = \frac{J_s(\omega_B)^2}{2S_B r^2}$ s or equivalently J_s MWs. Correspondingly, the FSD has a virtual kinetic energy $E_s = \frac{1}{2}J_s\omega_s^2$ at the virtual mechanical frequency $\omega_s = \frac{\omega_i\omega_B}{r}$, with r pairs of virtual poles, and will respond to the frequency deviation by:

$$-\Delta P_s = \dot{E}_s = J_s\omega_s\dot{\omega}_s \Leftrightarrow -\Delta p_s = 2H_s\omega_i\dot{\omega}_i \approx 2H_s\dot{\omega}_i \tag{2}$$

The control signals could be measured at the generator side (rotating speed) or the system side (frequency at the point of connection). Throughout this paper, we adopt the bus frequency as the control signal, but the proposed FSD control mechanism is general enough to allow for other sources of control signals. Furthermore, to obtain more realistic results, the storage dynamics, response time and communication delay are considered in the proposed simulation framework. We adopt the storage system with the controllers that regulate the dynamic response of the FSD [22], [23]. The local frequency ω_i is regulated through storage real power by a storage control module while the voltage at the point of connection with the grid is regulated through storage reactive power by a voltage control module.

In this paper, as shown in Fig. 1, a simplified dynamic behavior of the storage system is synthesized by two lag blocks with time constants: T_{fP} and T_{sP}. Specifically, the storage control module proposed in [22] is modified to provide inertial responses with $K_{sP} = -2H_s$.[2]

Here we provide a numerical example to illustrate the proposed control strategy of FSDs to mimic inertia. Considering a generation set of I conventional units, we utilize the primary frequency response analysis model [24], [25], shown in Fig. 2,

[1] p_{s0} (P_{s0}) is the storage output level determined in unit commitment or economic dispatch.

[2] As shown in [22], the storage performances using the simplified model are close to those using detailed models. Thus, it is proper to adopt this simplified storage model. For further detailed comparison of this simplified storage model with others, we refer readers to work [22].

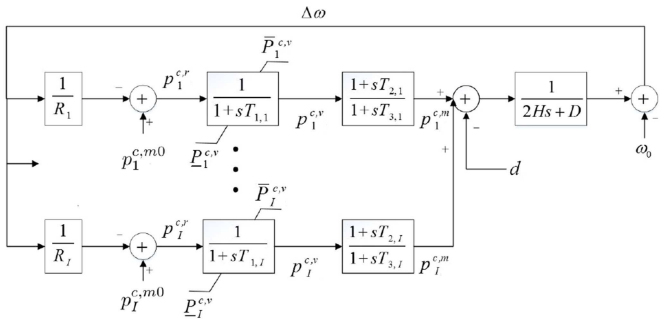

Fig. 2. Block diagram representation of a uniform frequency dynamic model.

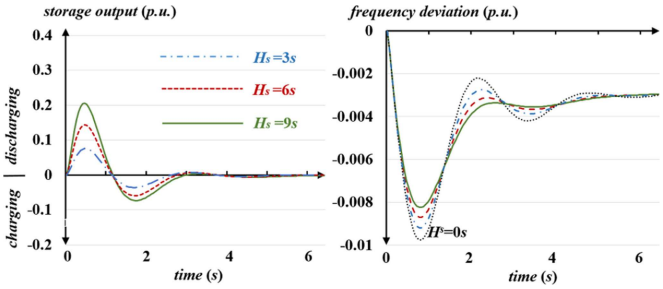

Fig. 3. Impacts of virtual inertia on power system PFR performances in consideration of FSD dynamics.

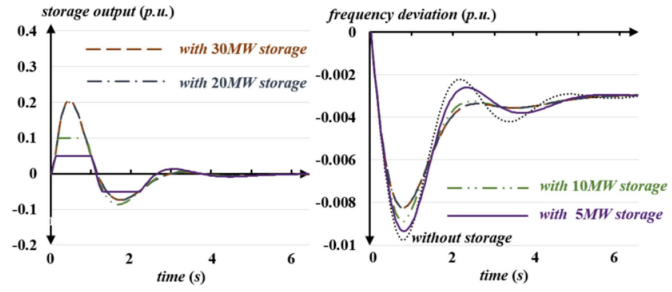

Fig. 4. Dynamic simulation considering the upper bounds on storage charging and discharging rates and FSD dynamics with $H_s = 9$ s.

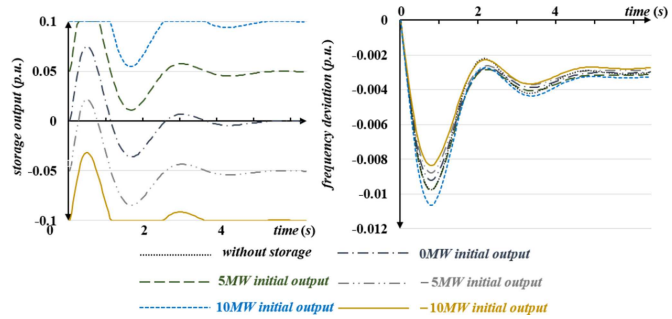

Fig. 5. Dynamic simulations with varying initial storage outputs in consideration of FSD dynamics.

which 1) ignores the network effects; 2) assumes all the generators move coherently as a single lumped mass; 3) assumes that system load damping behaviors are lumped together and modeled as a single constant. $p_i^{c,r}$ and $p_i^{c,v}$ are droop power order and governor valve position of each unit. The mechanical input of each unit is represented by $p_i^{c,m}$ with reference value to be $p_i^{c,m0}$. R_i denotes as the droop or regulation constant. We refer readers to [24], [25] for further information on this model. This system has 10 120-MW (=1.2 p.u.) conventional units with inertia varying from 3.5 s to 2.5 s, in the decrement of 0.1 s and time constants $T_{i,1} = 0.5$ s, $T_{i,2} = 2.5$ s and $T_{i,3} = 5.5$ s, respectively. We consider a contingency with a sudden load increase of 1 p.u. from the base load 10 p.u. and initial storage output of 0 p.u. $T_{fP} = 0.1$ s and $T_{sP} = 0.5$ s for all FSDs.

We present in Fig. 3 the storage outputs and frequency deviations *w.r.t.* different virtual inertia values in consideration of FSD dynamics. The higher the virtual inertia is, the better frequency response the system has. Correspondingly, a higher virtual inertia value requires a higher charging/discharging capacity for FSDs. As shown Fig. 4, when storage capacity is less than 30 MW, the improvement brought by the virtual inertia on the system PFR performances is reduced as the charging/discharging capacity decreases. Fig. 5 indicates that different storage initial outputs have significant impacts on the system PFR performances. The storage devices in charging status help the system arrest the frequency while those in discharging status further worsen the minimum frequency compared to the case without storage. Furthermore, we note that the storage with -10 MW initial output can contribute to the inertial responses right after the contingency occurs while the storage with 10 MW initial output starts to help arrest the frequency deviation only after the frequency has been dropping for a second. The observation is reasonable since FSDs have more headroom to respond to the decrease in frequency, when the storage device is withdrawing electricity from the grid.

III. The Minimum-Cost FSD Scheduling Problem

Unit commitment is typically run every 24 hours and economic dispatch is performed every 15 minutes [26]. After economic dispatch results for the next 15 minutes are determined, necessary control strategies need to be prepared for assuring system transient stability. To guarantee that the local post-contingency frequencies/RoCoFs are within their allowed ranges after each disturbance from a given set of contingency events (CEs), a scheduling problem is formulated in this section to find a minimum-cost commitment of multi-site FSDs. Underfrequency contingencies are represented in this work with both minimum frequency and maximum RoCoF limits, but the proposed method is general enough for taking other contingencies or limits into account. An accurate transient stability DAE model of the system is assumed to be available with sufficiently detailed information for both generation and demand sides.

A. FSD Scheduling Problem Formulation

Vector $\mathbf{x} = [x_1, x_2, \ldots, x_N]^T$ denotes the non-negative virtual inertias (decision variables in the optimization problem) provided by the FSDs, with upper bounds $\bar{\mathbf{H}} = [\bar{H}_1, \bar{H}_2, \ldots, \bar{H}_N]^T$ and lower bounds $\underline{\mathbf{H}} = [\underline{H}_1, \underline{H}_2, \ldots, \underline{H}_N]^T$. We define $\mathcal{N} = \{1, 2, \ldots, N\}$. Given the set $\mathcal{E}$ including E CEs of interest and the marginal costs $\mathbf{c}$ for virtual inertias $\mathbf{x}$, a non-linear scheduling problem for multi-site FSDs is formulated

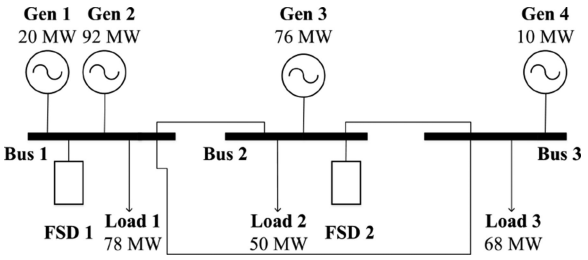

Fig. 6. Three-bus case one line diagram.

to assure that minimum frequency $f_{b,e}^{\min}|_{\mathbf{x}}$ and maximum RoCoF magnitude $r_{b,e}^{\max}|_{\mathbf{x}}$ of each bus $b \in \mathcal{B}$ for any contingency $e \in \mathcal{E}$ are within the limits $\underline{f}_b$ and $\bar{r}_b$, respectively:

$$\min_{\mathbf{x}} : \mathbf{c}^T \mathbf{x} \tag{3a}$$

$$s.t.: f_{b,e}^{\min}|_{\mathbf{x}} \geq \underline{f}_b, \text{ for } \forall b \in \mathcal{B}, e \in \mathcal{E} \tag{3b}$$

$$r_{b,e}^{\max}|_{\mathbf{x}} \leq \bar{r}_b, \text{ for } \forall b \in \mathcal{B}, e \in \mathcal{E} \tag{3c}$$

$$x_n \in \{0, [\underline{H}_n, \bar{H}_n]\}, \text{ for } \forall n \in \mathcal{N} \tag{3d}$$

B. Illustrative Example

A three-bus case, as shown in Fig. 6, illustrates the nonlinear minimum-cost FSD ($|\mathcal{N}| = 2$) commitment problem, in consideration of a single CE $\mathcal{E} = \{''\text{the loss of unit 4}''\}$ and a single constrained bus $\mathcal{B} = \{''\text{bus 2}''\}$. Each FSD has a charging/discharging capacity of 20 MW with $\bar{\mathbf{H}} = [10, 8]^T$ and $\underline{\mathbf{H}} = [0, 0]^T$. A uniform price[3] of \$200/s for the inertial services is adopted in this example [9][4]. The minimum frequency limit is set to 59.5 Hz and the maximum RoCoF limit is 0.5 Hz/s, as measured over a rolling 500ms period [27].

Fig. 7 displays the the maximum RoCoF (left) and minimum frequency (right) for bus 2 over $x_1 - x_2$ space with the feasible and infeasible regions separated by the boundaries, which are indicated using broken (left) and solid (right) curves. The curved and asymmetric boundaries verify the locational impacts of the virtual inertia services and the nonlinear relationship between the selected metrics and the provided inertia. As shown in Fig. 8, the two boundaries are combined to obtain the feasible region (lightblue) of inertia services for maintaining both minimum frequency and maximum RoCoF of bus 2 within their bounds. Given the marginal costs of of virtual inertias provided by FSDs, the minimum commitment cost is \$1620 when $\mathbf{H} = [5, 3.1]^T$.

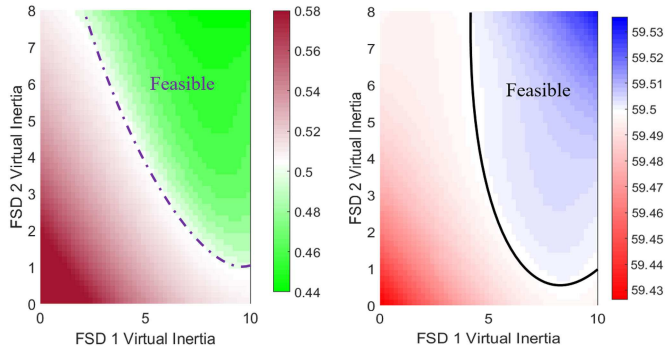

Fig. 7. The max. RoCoF and min. frequency for bus 2 over $x_1 - x_2$ space.

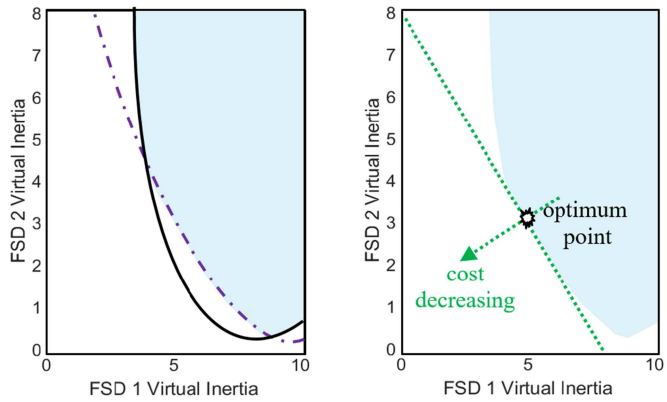

Fig. 8. Feasible region over $x_1 - x_2$ space.

IV. An Iterative Solution Algorithm

A search in the solution space for the optimal feasible solutions, with J possible values for each FSD, requires $\mathcal{O}(EJ^N)$ of full transient stability simulations, which is very computationally intensive. Thus, a generic search in the solution space is almost impossible for practical applications. In order to reduce computational burdens, we present in this section a computationally tractable algorithm for this scheduling problem. As shown in Figs. 9 and 10, linearizion can be used to approximate the contributions of the virtual inertia from FSD to the bus minimum frequencies and maximum RoCoFs with an appropriate level of accuracy. Specifically, an iterative algorithm is proposed to formulate and update a MILP problem with linearized frequency constraints, and then to find the minimum-cost commitment of FSDs. For the remaining sections, nomenclature is presented at the end of this paper.

[3]The objective function coefficient c_n could be any reasonable value. For instance, if all coefficients are set to 1, the objective function aims to minimize the total virtual inertia values committed to satisfy the minimum frequency and maximum RoCoF magnitude requirements after contingencies of interest. Cost analysis could also be performed to assign a value to c_n by considering storage installation costs, operational wear and tear.

Currently, there is not an effective market framework that provides economic incentives for market participants to offer (virtual) inertia services. In [9], we perform modifications essential to integrate system dynamic model into security-constrained unit commitment models for the assessment of economic values of the provided inertia services. The proposed evaluation framework includes three steps: 1) discretizing the dynamic simulation model; 2) integrating the discrete-time dynamic model into the steady-state unit commitment model as transient-stability security constraints; and 3) transforming nonlinear constraints into equivalent, linear forms. To compute the economic value of additional inertia, we perform simulations twice on the same system, changing only the total virtual inertia value by a certain amount. The ratio of the production cost decrement to the virtual inertia increment approximates the system-wise average inertia value, which forms the basis to determine the price for each FSD to provide virtual inertia. Each FSD has its own price, different from the system-wise average price for inertia, due to factors such as various lifetimes, technologies, maintenance and operation costs, and so on. Therefore, in this work, we consider the cost variation of virtual inertia services from multiple locations over the grid.

[4]A base of 100 MVA is used for all FSDs in this section. As such, for virtual inertia services, 200 \$/s and 2 \$/MWs conceptually represent the same price for a FSD. For instance, to deploy a FSD that provides 2-s (equivalently 200-MWs) virtual inertia, the deployment cost could be given in either way: 200 \$/s $*$ 2 s $=$ 400\$ $=$ 2 \$/MWs $*$ 200 MWs.

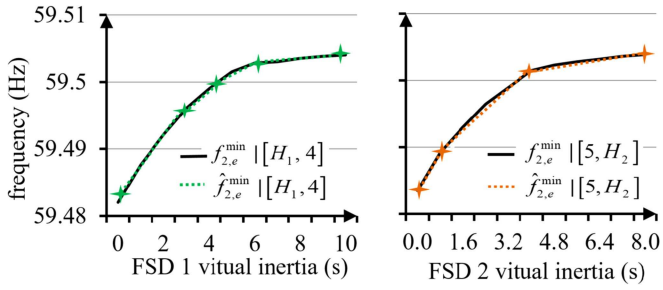

Fig. 9. Three-bus case bus 2 minimum frequency and its linearization.

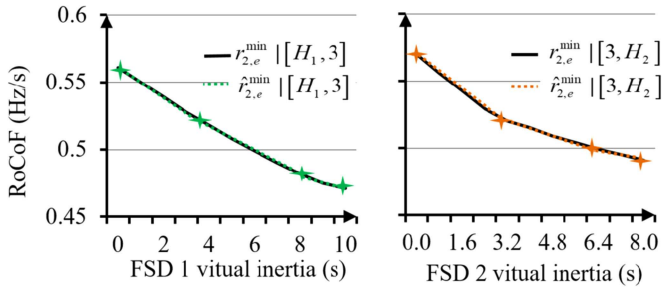

Fig. 10. Three-bus case bus 2 maximum RoCoF and its linearization.

A. Linearized Scheduling Problem Formulation

Given the virtual inertia bounds $\underline{\mathbf{H}} \le \mathbf{x} \le \bar{\mathbf{H}}$, each solution region $\{x_n : \underline{H}_n \le x_n \le \bar{H}_n\}$ is partitioned into $\bar{Z}_n$ segments. For FSD n, the virtual inertia values of interest are represented by the $(\bar{Z}_n+1)\times 1$ vector $\mathbf{h}_n = [h_{n,0} = \underline{H}_n, h_{n,1}, \ldots, h_{n,\bar{Z}_n} = \bar{H}_n]^T$. We denote the current virtual inertia setting as $\mathbf{H} = [h_1, h_2, \ldots, h_N]^T$. The vector $\hat{\mathbf{H}}_{n,z} = [\ldots, h_{n,z}, \ldots]$ differs from $\mathbf{H} = [\ldots, h_n, \ldots]^T$ only by the virtual inertia setting for FSD n. Specifically, we define $\hat{\mathbf{H}}_{n,-1} = [\ldots h_{n-1}, 0, h_{n+1}, \ldots]^T$ with $h_{n,-1} = 0$ and $\mathcal{Z}_n = \{0, 1, \ldots, \bar{Z}_n\}$. Let $m \in \mathcal{M} = \{f^{\min}, (-r)^{\max}\}$ be the metrics of interest and $M_b \in \{\underline{f}_b, -\bar{r}_b\}$ represents the corresponding limits for bus b. Then, the marginal benefit measure to commit the virtual inertia of the segment z for the FSD n is given in (4a). The equivalent frequency/RoCoF requirement measures are defined in (4b). Given the current commitment plan $\mathbf{H}$, $\Delta h_{n,z}$ defined in (4c) represents the value of committed inertia in $\mathbf{H}$ from segment $[h_{n,z-1}, h_{n,z}]$. The parameter definitions are visually represented in Fig. 11.

$$a^m_{b,e,n}[z]|_{\mathbf{H}} = \frac{m_{b,e}|_{\hat{\mathbf{H}}_{n,z}} - m_{b,e}|_{\hat{\mathbf{H}}_{n,z-1}}}{h_{n,z} - h_{n,z-1}}, \text{ for } z \in \mathcal{Z}_n \tag{4a}$$

$$v^m_{b,e}|_{\mathbf{H}} = M_b - m_{b,e}|_{\mathbf{H}} \tag{4b}$$

$$\Delta h_{n,z} = \begin{cases} h_{n,z} - h_{n,z-1}, & \text{if } h_{n,z} \le h_n \\ 0, & \text{if } h_n \le h_{n,z-1} \\ h_n - h_{n,z-1}, & \text{otherwise} \end{cases} \tag{4c}$$

Thus, the linearized scheduling problem with $\sum_{n=1}^{N}(\bar{Z}_n+1)$ continuous variables $d_{n,z}$ and $\sum_{n=1}^{N}(\bar{Z}_n+1)$ binary variables $u_{n,z}$ is formulated in (5) where $\mathbf{d} = [\sum_{z=0}^{\bar{Z}_1} d_{1,z}, \sum_{z=0}^{\bar{Z}_2} d_{2,z}, \ldots, \sum_{z=0}^{\bar{Z}_N} d_{N,z}]$. The objective function (5a) is to minimize the total commitment costs for all FSDs. In constraint (5b), $a^m_{b,e,n}[z]|_{\mathbf{H}} d_{n,z}$ (or $a^m_{b,e,n}[z]|_{\mathbf{H}} \Delta h_{n,z}$) is the linearized contribution of the commitment of segment z of FSD n with its committed virtual inertia to be $d_{n,z}$ (or $\Delta h_{n,z}$). Thus, $\sum_{n\in\mathcal{N}, z\in\mathcal{Z}_n} a^m_{b,e,n}[z]|_{\mathbf{H}}(d_{n,z} - \Delta h_{n,z})$ is the linearized improvement on the metrics of interest, compared to those conditioned on the current commitment plan $\mathbf{H}$, and $v^m_{b,e}|_{\mathbf{H}}$ is the minimum improvement needed such that each metric is within its limit. Constraint (5d) represents the upper limit of the committed inertia $d_{n,z}$ from segment z. Constraints (5d) and (5e) indicate each FSD cannot provide the virtual inertia of a value between zero and $\underline{H}_n$. Segment $z+1$ can provide inertia only when the segment z has offered all its available inertia $h_{n,z} - h_{n,z-1}$, which is included in this problem by (5f).

$$\min_{\mathbf{d},\mathbf{u}}: \mathbf{c}^T\mathbf{d} \tag{5a}$$

$$s.t.: \text{ for } \forall b \in \mathcal{B}, e \in \mathcal{E}, m \in \mathcal{M}$$

$$\sum_{n\in\mathcal{N}, z\in\mathcal{Z}_n} a^m_{b,e,n}[z]|_{\mathbf{H}}(d_{n,z} - \Delta h_{n,z}) \ge v^m_{b,e}|_{\mathbf{H}} \tag{5b}$$

$$\text{for } \forall b \in \mathcal{B}, e \in \mathcal{E}, z \in \mathcal{Z}_n, n \in \mathcal{N}$$

$$u_{n,z} \in \{0,1\} \tag{5c}$$

$$d_{n,z} \le u_{n,z}(h_{n,z} - h_{n,z-1}) \tag{5d}$$

$$u_{n,0} h_{n,0} \le d_{n,0} \tag{5e}$$

$$u_{n,z+1}(h_{n,z} - h_{n,z-1}) \le d_{n,z}, \quad z \ne \bar{Z}_n \tag{5f}$$

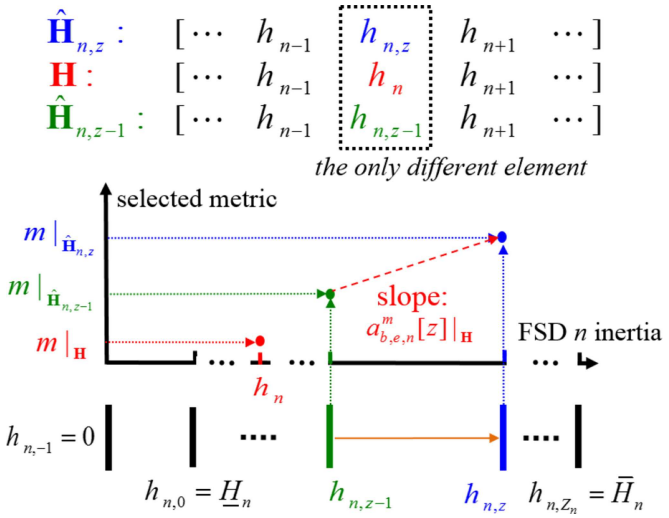

Fig. 11. Visual representation of the parameter setting up.

B. Iterative Solution Algorithm

The linearized minimum-cost commitment problem facilitates an iterative solution algorithm - a two-loop iterative solution technique - shown in Table I. Generally speaking, the outer loop, indexed by s, updates the solution space center and shrinks the solution space. The inner loop, indexed by k, increases the requirement measures for cases when minimum

TABLE I
ITERATIVE SOLUTION ALGORITHM

1.A	Set $s=1$ and initialize $\mathbf{H}^{(s)}$ by $\mathbf{d}^{*(0,1)}$; Set $\hat{s}=0$ and $\hat{\mathcal{S}}=\{\}$;
2.A	Set $k=1$; Compute the $a^{m}_{b,e,n}[z]\|_{\mathbf{H}^{(s)}}$ - benefit measures conditioned on $\mathbf{H}^{(s)}$ - using (4a) and $v^{m(s,k)}_{b,e}=v^{m}_{b,e}\|_{\mathbf{H}^{(s)}}$ - the requirement measures conditioned on $\mathbf{H}^{(s)}$ - using (4b), where $\mathbf{H}^{(s)}$ is obtained using $\mathbf{d}^{*(s-1,K_{s-1})}$;
2.B	Formulate the MILP (5) to solve $\mathbf{d}^{*(s,k)}$;
2.C	Use full dynamic model to compute $m_{b,e}\|_{\mathbf{d}^{*(s,k)}}$;
2.D	If no frequency limits violate, go to Step 4.A; Else, continue;
3.A	Increment k; Update the frequency/RoCoF requirement measure using (6) for violated constraints in (5b);
3.B	Go to Step 2.B;
4.A	Set $K_s=k$;
4.B	If $\mathbf{c}^T\mathbf{d}^{*(s,K_s)}\le\mathbf{c}^T\mathbf{d}^{*(s',K_{s'})}$ for $s'\in\hat{\mathcal{S}}$, record $\mathbf{d}^{*(s,K_s)}$ and continue; Else, go to Step 4.D;
4.C	If $\|\mathbf{c}^T\mathbf{d}^{*(s,K_s)}-\mathbf{c}^T\mathbf{d}^{*(\hat{s},K_{\hat{s}})}\|>\epsilon$, $\hat{s}=s$ and $\hat{\mathcal{S}}=\hat{\mathcal{S}}\bigcup\{\hat{s}\}$ and continue; Else, go to Step 4.E;
4.D	If $s+1$ is within limit, update solution space using (7), increase s and go to Step 2.A; Else, continue;
4.E	Record $\mathbf{d}^{*(s,K_s)}$ as the final solution; **End** of the algorithm.

frequency/maximum RoCoF computed using full transient stability model violate their pre-determined bounds.

Within each outer loop s, we repeatedly update the equivalent frequency/RoCoF requirement measures using (6) to strengthen the limits violated by the previous optimum solution $\mathbf{d}^{*(s,k-1)}$ until the computed minimum frequency/maximum RoCoF conditioned on $\mathbf{d}^{*(s,k)}$ satisfy all the requirements for all the contingencies of interest.

$$v^{m(s,k)}_{b,e}=v^{m(s,k-1)}_{b,e}+\beta^{m(s,k)}_{b,e}\left(M_b-m_{b,e}|_{\mathbf{d}^{*(s,k-1)}}\right) \quad (6)$$

At the end of each outer loop s, the algorithm updates the solution space center $\mathbf{H}^{(s+1)}$ using the optimum solution $\mathbf{d}^{*}|_{\mathbf{H}^{(s,K_s)}}=\mathbf{d}^{*(s,K_s)}$. To guarantee the convergence of the proposed algorithm, we apply a factor $\alpha^{(s)}_n$ to shrink the solution space by (7). Again, the virtual inertia space of each FSD n in a new solution space is partitioned into $\bar{Z}_n$ segments. Then, the marginal benefit and equivalent requirement measures are computed to formulate (5) conditioned on $\mathbf{H}^{(s+1)}$ for later simulations.

$$h^{(s+1)}_{n,0}=\max\left\{\underline{H}_n, d^{*(s,K_s)}_n-\frac{\alpha^{(s)}_n}{2}\left(h^{(s)}_{n,\bar{Z}_n}-h^{(s)}_{n,0}\right)\right\} \quad (7a)$$

$$h^{(s+1)}_{n,\bar{Z}_n}=\min\left\{\bar{H}_n, d^{*(s,K_s)}_n+\frac{\alpha^{(s)}_n}{2}\left(h^{(s)}_{n,\bar{Z}_n}-h^{(s)}_{n,0}\right)\right\} \quad (7b)$$

C. Computational Burden

Suppose that there are S outer loops and each outer loop has K_s inner loops until the end of the algorithm. Since Step 2.A and 2.C require $E\sum_{n=1}^{N}(\bar{Z}_n+2)$ and E simulations using the full dynamic model, respectively. The proposed algorithm needs to run full transient stability simulation for $\sum_{s=1}^{S}E(\sum_{n=1}^{N}\bar{Z}_n+K_s+2N)$ times. Assume that $\bar{Z}_n+2$ and K_s are bounded by Z and K, respectively. The proposed iterative solution algorithm requires $\mathcal{O}(SE(NZ+K))$ of full transient stability simulations.

V. SENSITIVITY-BASED ITERATIVE ALGORITHM

The computational burden in the iterative solution algorithm mainly comes from 2.A, which requires $E\sum_{n=1}^{N}(\bar{Z}_n+2)$ simulations to compute the marginal benefit measures $a^{m}_{b,e,n}[z]|_{\mathbf{H}^{(s)}}$. In this section, we propose a sensitivity-based approach to approximate the marginal benefit measures.

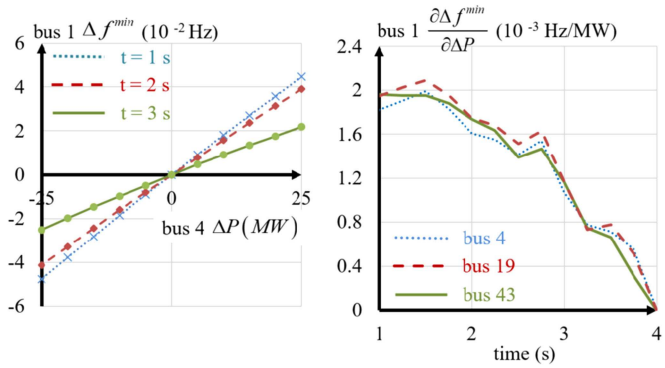

Fig. 12. Bus 1 minimum frequency change v.s. additional real power injection.

A. Sensitivity Analysis

Given the IEEE 118-bus test case [28], [29] with a total load of 5242 MW and a total installed generation capacity of 8935 MW, we consider a single contingency event with the loss of the conventional unit (output: 554 MW) on bus 69 ($e=69$) at time of 1s and measure the post-contingency frequencies/RoCoFs of bus 1 ($b=1$) over multiple scenarios.

First, Fig. 12 (left) shows the $\Delta f^{\min}_{b,e}$ w.r.t. the power injections ΔP from bus 4 at time 1s, 2s and 3s. The results clearly show that the minimum frequency changes in a nearly linear fashion as the power injection ΔP. Then, the minimum frequency sensitivity to power injection at several dispersed locations are computed and the computed $\frac{\partial \Delta f^{\min}_{b,e}}{\partial \Delta p}=\frac{\partial f^{\min}_{b,e}}{\partial p}$ are presented in Fig. 12 (right). We observe a non-linear behavior of $\frac{\partial f^{\min}_{b,e}}{\partial p}$ w.r.t. time and the location-dependent of $\frac{\partial f^{\min}_{b,e}}{\partial p}$ at each specific time. Similar results are observed in Fig. 13 for the maximum RoCoF as well. For locational variation, we consider bus 4 (2 nodes away from bus 1), bus 19 (4 nodes away from bus 1) and bus 43 (6 nodes away from bus 1). Then Fig. 14 also displays the time-dependent change in the selected metrics on bus 1 w.r.t. the reactive power injection change at bus 4.

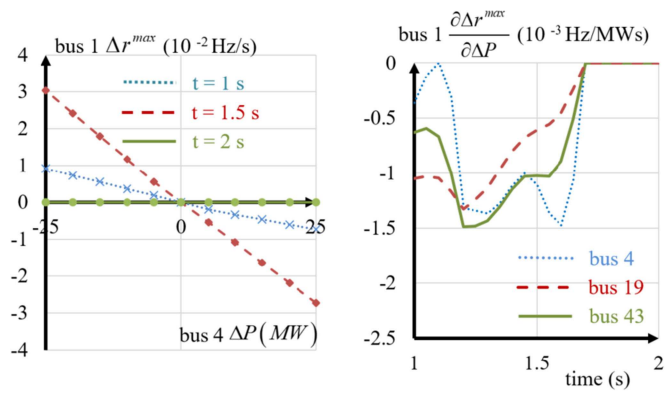

Fig. 13. Change of bus 1 maximum RoCoF v.s. additional real power injection.

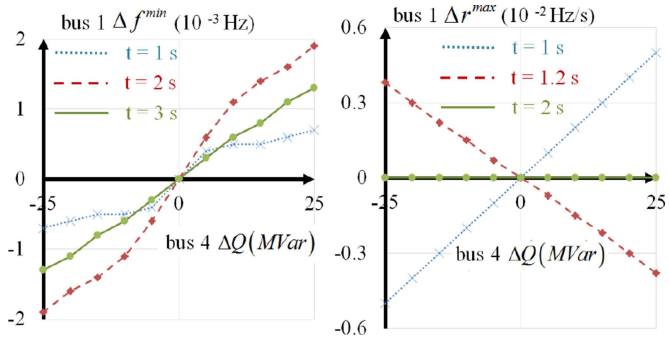

Fig. 14. Time-dependent change in selected metrics on bus 1 v.s. additional reactive power injection from bus 4.

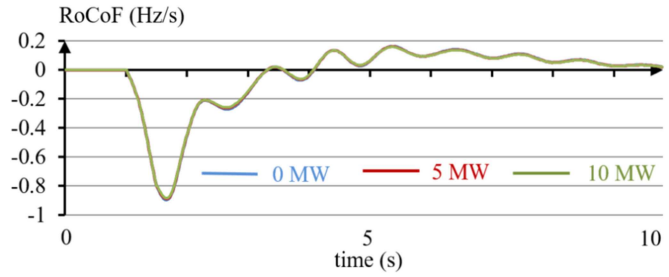

Fig. 15. Bus 1 RoCoF v.s. additional real power injection from bus 4.

Furthermore, we consider the real power injection change in bus 4 at time 1.5 s with a value of 0-, 5- and 10-MW, respectively. The indistinguishable curves in Fig. 15 verify that the power outputs from each FSD have a small impact on the system frequency. Thus, it is appropriate to estimate the contribution of each segment of every FSD through the playback of the frequency measurements at each bus.

B. Sensitivity-Based Benefit Measure Estimation

Based on the assumption that the commitment of each individual FSD n has trivial impacts on the power system dynamic responses, each FSD is the only source with substantial changes in its power outputs. Assuming that the frequency response of each bus is linear with respect to real and reactive power injections at any instant in time, the marginal benefit measures can be estimated by

$$a^m_{b,e,n}[z]|_{\mathbf{H}} \approx \frac{\int_{\tau=t_0}^{t_{e,end}} [\frac{\partial m_{b,e}|_{\mathbf{H}}}{\partial p^s_n} \frac{d\Delta p^s_n|_z}{dt} + \frac{\partial m_{b,e}|_{\mathbf{H}}}{\partial q^s_n} \frac{d\Delta q^s_n|_z}{dt}] d\tau}{h_{n,z} - h_{n,z-1}} \tag{8}$$

where the t_0 is the time when the CE e occurs and $t_{e,end}$ is the time when the last bus in the system has reached its minimum frequency, and $\Delta p^s_n|_z = p^s_n|_z - p^s_n|_{z-1}$. On one hand, we can approximate p^s_n and q^s_n by $\tilde{p}^s_n$ and $\tilde{q}^s_n$ through the playback of the frequency measurements at each bus with the given virtual inertia value. On the other hand, we partition the period $[t_0, t_{e,end}]$ into T_e segments to linearize $\frac{\partial m_{b,e}|_{\mathbf{H}}}{\partial p^s_n}$ and $\frac{\partial m_{b,e}|_{\mathbf{H}}}{\partial q^s_n}$ into $S^m_{b,e,n}(t)|_{\mathbf{H}}$ and $G^m_{b,e,n}(t)|_{\mathbf{H}}$. Specifically, we perform full dynamic simulation to compute $S^m_{b,e,n}(t)|_{\mathbf{H}}$ and $G^m_{b,e,n}(t)|_{\mathbf{H}}$ for those selected time points and linearly interpolate the sensitivity measures for values between selected time points. Correspondingly, the marginal benefit measures can be approximated by

$$\tilde{a}^m_{b,e,n}[z]|_{\mathbf{H}} \approx \frac{\int_{\tau=t_0}^{t_{e,end}} [S^m_{b,e,n}|_{\mathbf{H}} \frac{d\Delta \tilde{p}^s_n|_z}{dt} + G^m_{b,e,n}|_{\mathbf{H}} \frac{d\Delta \tilde{q}^s_n|_z}{dt}] d\tau}{h_{n,z} - h_{n,z-1}} \tag{9}$$

Using the approximated marginal benefit measures, we can further compute the approximated frequency/RoCoF requirement measures $\tilde{v}^m_{b,e}|_{\mathbf{H}}$. Finally, the iterative solution algorithm presented in Section IV is modified into the sensitivity-based approach, detailed in Table II. Since the frequency is more dependent on the real power balance, $G^m_{b,e,n}|_{\mathbf{H}} = 0$ is assumed to further reduce computational complexity.

C. Computational Burden

Suppose that there are S outer loops and each outer loop has K_s inner loops until the end of the algorithm. Step 2.$\tilde{\text{A}}_1$ and 2.C require $R\sum_{e=1}^{E} T_e$ and E simulations using the full dynamic model, respectively. $R \leq N$ is the number of buses where the N FSDs are installed. The proposed algorithm needs to run the transient stability model for $\sum_{s=1}^{S}(EK_s + R\sum_{e=1}^{E} T_e)$ times. Assume that T_e and K_s are bounded by T and K, respectively. The proposed iterative solution algorithm requires $\mathcal{O}(SE(RT+K))$ of full transient stability simulations. In addition, the buses can be grouped into several clusters with similar dynamic behaviors [30], [31], then we only need to perform sensitivity analysis on $R' < R$ regions with the computational burden reduced to $\mathcal{O}(SE(R'T+K))$ of full transient stability simulations. Similarly, if the locations of multiple contingencies are close to each other, we can group those contingencies into one category, represented by the worst case in that group. In such way, we can further lower the computational burden to $\mathcal{O}(SE'(R'T+K))$, where E' is the number of contingency clusters.

This paper primarily focuses on solving the nonlinear optimization problem (3). Actually, such a minimization problem could not be formulated and solved as a regular optimization problem, since the minimum frequency and maximum RoCoF magnitudes could be computed only by running dynamic simulations. Thus, we develop an algorithm to effectively solve the

TABLE II
SENSITIVITY-BASED ITERATIVE SOLUTION ALGORITHM

1.A	Set $s = 1$ and initialize $\mathbf{H}^{(s)}$ by $\mathbf{d}^{*(0,1)}$; Set $\hat{s} = 0$ and $\hat{\mathcal{S}} = \{\}$;
2.$\tilde{\text{A}}_1$	Set $k = 1$; Compute the sensitivity measures $S^m_{b,e,n}\|_{\mathbf{H}^{(s)}}$, $G^m_{b,e,n}\|_{\mathbf{H}^{(s)}}$;
2.$\tilde{\text{A}}_2$	Compute the benefit measures $\tilde{a}^m_{b,e,n}[z]\|_{\mathbf{H}^{(s)}}$ conditioned on $\mathbf{H}^{(s)}$ using (9) and the requirement measures $\tilde{v}^{m(s,k)}_{b,e}$ conditioned on $\mathbf{H}^{(s)}$ using (4b);
2.B-4.E	The same as *Iterative Solution Algorithm*.

TABLE III
SELECTED FSD CONFIGURATIONS

$\bar{H}$(s)	5	7	6	11	20	12	8	14
$\underline{H}$(s)	0	0	0	0	0	0	0	0
costs($/s)	93	108	105	92	79	55	71	102
bus index	10	12	25	26	27	62	67	69

optimization problem, but this algorithm is general enough to consider other FSD control algorithms.

VI. ILLUSTRATIVE SIMULATION STUDIES

In this work, we perform extensive studies on the modified 118-bus test system used in Section V [28], [29] to verify the potential computational benefits of the proposed iterative solution approach and sensitivity-based method. The storage dynamic model used in Section II is adopted here with power capacity to be 15 MW for all FSDs. All FSDs are assumed to have zero initial power output. Since primary frequency covers up to tens of seconds, thus we assume energy capabilities for all FSDs are sufficiently large[5].

We consider four under-frequency contingencies ($E = 4$), each of which simulates the loss of one generator. The four generators are sited at bus 80 (389 MW), bus 100 (415 MW), bus 61 (386 MW) and bus 59 (423 MW), respectively. A minimum frequency limit of 59.5 Hz and a maximum RoCoF limit of 0.5 Hz/s over a 500-ms period are considered for all the buses ($|\mathcal{B}| = 118$). Each generator adopts either GENSAL or GENROU machine model, and either EXST1, EXST2 or IEEET1 exciter model. We consider either IEEEG1, GAST, HYGOV or TGOV1 as each generator's governor model. All models use default parameters on an MVA base equal to 125% of their respective MW capacity [32]. Finally, all loads are modeled with the constant impedance model. We consider the installation of one single FSD at each selected bus ($|\mathcal{N}| = R = 33$), with the corresponding parameters for a portion of FSDs given in Table III. Without any FSD commitment, the simulated system frequency response results in a minimum frequency of 59.366 Hz and in a maximum RoCoF of 0.803 Hz/s.

The proposed approach is modified into ten different cases, as shown in Table IV. In cases 1−4, we use actual data to compute

[5]Take a FSD with 15-MW charging/discharging capacity as an example. If this FSD is charged or discharged over a 20-second primary frequency response simulation period, the change of its storage energy is no more than 300 MWs $<$ 0.1 MWh, which is significantly smaller than typical FSD capabilities [33].

TABLE IV
TEST CASE SOLUTION METHOD SPECIFICATION AND RESULTS

case	measure	Z	T	R'	costs ($)	# of simulations
1	actual	8	N/A	N/A	9155	5332
2	actual	5	N/A	N/A	9173	3340
3	actual	3	N/A	N/A	9327	2032
4	actual	2	N/A	N/A	9645	1364
5	estimated	5	10	33	9163	7972
6	estimated	5	10	11	9208	2696
7	estimated	5	10	3	9342	780
8	estimated	5	5	3	9363	488
9	estimated	5	5	3	9364	282 ($E' = 2$)
10	estimated	5	5	3	9388	224 ($E' = 2$)

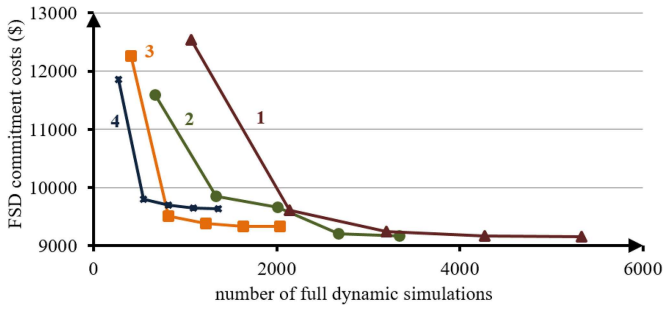

Fig. 16. Algorithm solution paths for cases 1−4.

marginal benefits $a^m_{b,e,n}[z]|_{\mathbf{H}}$ and requirement measures $v^m_{b,e}|_{\mathbf{H}}$. Specifically, the only variation in cases 1−4 is $\bar{Z}_n$ - the number of segments for each FSD's inertia range. Case 4 is a special case where one single benefit measure is adopted for each FSD n. For comparison purposes, we run cases 5−10 with $Z = 5$ and additionally adopt the sensitivity-based measures. Since frequency is more dependent on the real power balance, $G^m_{b,e,n}|_{\mathbf{H}} = 0$ is assumed in cases 5−10. In detail, cases 5−7 and 8−10 consider T to be 10 and 5, respectively. Case 6 adopts the regional sensitivity measures with $R' = 11$, while cases 7−9 have a value of 3 for R'. Additionally, we cluster the four contingencies into two groups ($E' = 2$) based on contingency locations. Compared to cases 1−9, case 10 adopts an adaptive method to update $\beta^{m(s,k)}_{b,e}$ at the end of each inner loop.

At first, Fig. 16 shows the solution path of the FSD commitment costs w.r.t. the number of full transient stability simulations. The marker of each line indicates the end of one outer loop with a feasible solution to be recorded. We note that the increasing number of segments lowers the final commitment costs, which converges to about $9200 when Z becomes higher

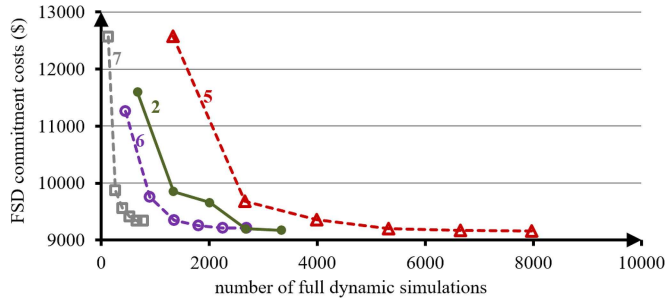

Fig. 17. Algorithm solution paths for cases 5−7.

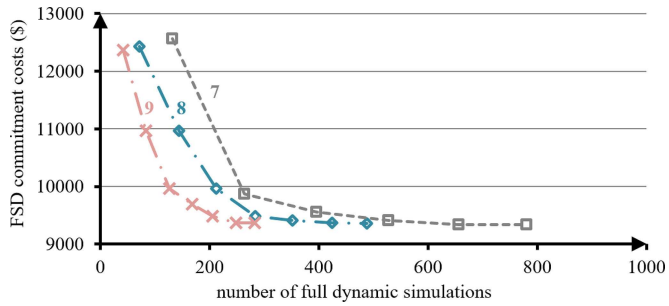

Fig. 18. Algorithm solution paths for cases 7–9.

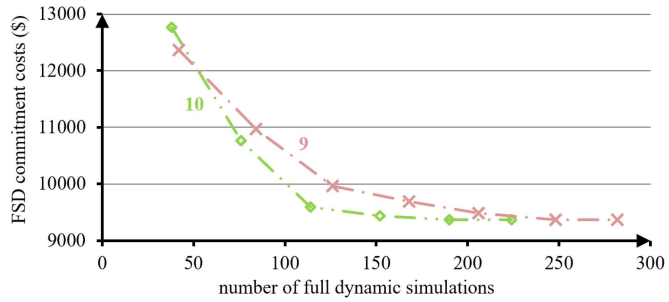

Fig. 19. Algorithm solution paths for cases 9–10.

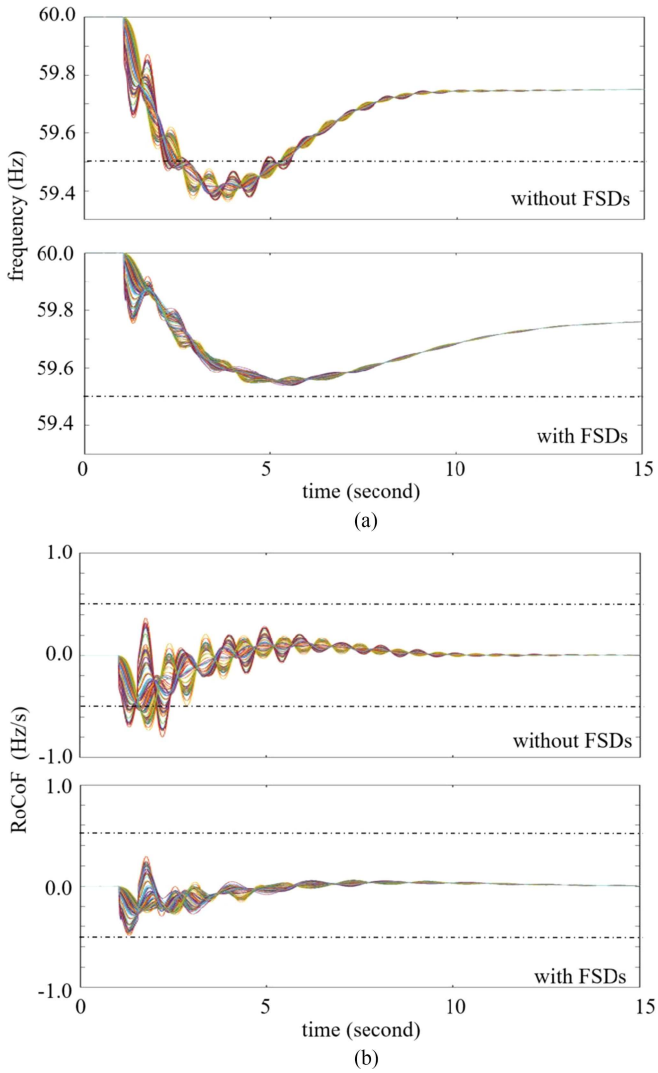

Fig. 20. Worst-scenario simulation results before and after deployment of FSDs in case 10. (a) Post-contingency frequency at each bus. (b) Post-contingency RoCoF at each bus.

than some value (5 in our case). As shown in Figs. 9 and 10, the impacts of the mimicked inertia behave in a nonlinear fashion as the virtual inertia increases. Thus, a higher number of segments can capture a more accurate linearized representation of the FSD impacts on the selected metrics. However, the selection of Z faces at the trade-off between computation accuracy and computation complexity. As Z increases, the computation becomes more burdensome. The results are reasonable since each increment in Z requires at lease EN full simulations per outer loop. With higher Z, the finer segmentation helps the algorithm's convergence. However, the finer segmentation can only slow down - not stop or reverse - the increasing number of full dynamic simulations as Z increases.

Then, T is set to 10 in cases 5−7 and 5 in cases 8−9 because of the nonlinear time dependence of sensitivity measures $S^m_{b,e,n}|_{\mathbf{H}}$. Fig. 17 presents the convergence path of the FSD commitment costs w.r.t. the number of full transient stability simulations to investigate the impacts of sensitivity measures with varying R'. Case 5 does not partition the FSDs into clusters ($R' = N$) and has almost the same commitment costs as case 2, which verifies the correctness of the proposed sensitivity-based approach. However, case 5 requires more full stability simulations than that of case 2 because of $TR' = 330 > NZ = 165$. Since each FSD has a small impact on frequency response and neighboring FSDs create similar effects on the system frequency responses, the time-varying frequency signals are used to cluster buses, where FSDs are sited, into R' groups, in each of which the buses have similar frequency curves. The clustering results are updated at the end of each inner loop. As the R' changes from 33 to 11 and then to 3, the decreasing computation complexity with slight change in the commitment cost verifies the effectiveness of the proposed sensitivity-based method to search in the feasible space for the optimal solution.

To further reduce the required number of full dynamic simulations, the T is reduced in cases 8−9 to 5 and the final commitment costs are slightly higher than that of case 7, as shown in Fig. 18. However, cases 8 and 9 require much fewer full

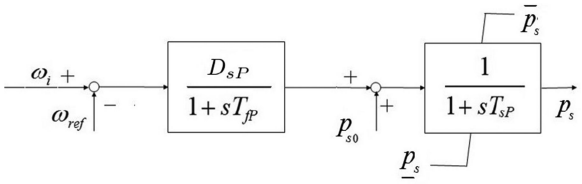

Fig. 21. Simplified structure of the storage system under droop control.

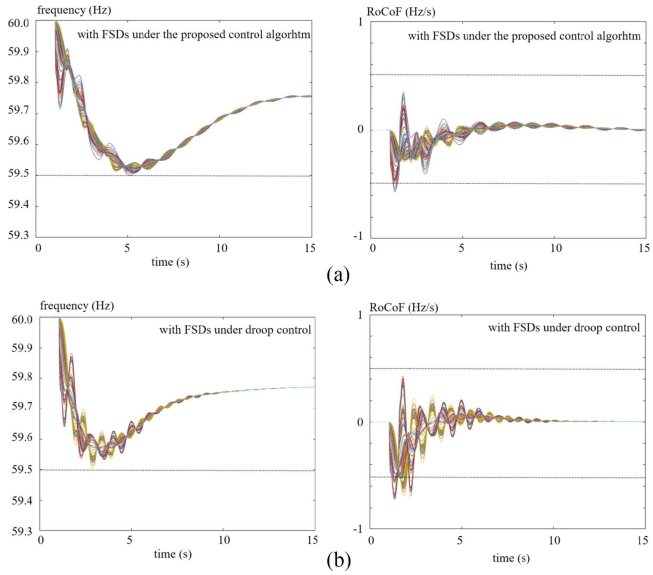

Fig. 22. Worst-scenario simulation results in case 10 after applying (a) the proposed control algorithm and (b) droop control, in consideration only of the minimum frequency constraint.

transient stability simulations. Unlike case 8, case 9 has a second factor causing the decrease in computational burden - the consideration that a group of contingencies close to each other have similar impacts on power system frequencies. Thus, their impacts can be represented by the regional worst contingency in each group. In our work, the bus 80 is one bus away from bus 100 and bus 61 is connected to bus 59. Therefore, we can group the four contingencies into $E' = 2$ groups (buses 80 with 100, and buses 61 with 59). These two groups of contingencies are 6 nodes away from each other.

To speed up the convergence of the algorithm, we apply a factor η_β larger than 1 in (6) to update $\beta_{b,e}^{m(s,k)} = \beta_{b,e}^{m(s,k-1)} * \eta_\beta$ when $M_b - m_{b,e}|_{d^{*(s,k-1)}}$ becomes very small (0.01 in our work) and the algorithm updates the solution in a very slow speed. As shown in Fig. 19, the case 10 with the adaptive updating rule facilitate the computation speed and requires only less inner loops for convergence. We present in Fig. 20 the transient stability simulation results without and with FSDs in the worst scenario of case 10. The simulation results show that the deployment of FSDs helps the grid satisfy minimum frequency and maximum RoCoF magnitude requirements at each bus.

In summary, given economic dispatch results for the next operation horizon, the iterative algorithm proposed in this work determines necessary virtual inertia services, while minimizing the total deployment costs, in a reasonable time. The results presented in Table IV show that reasonable solutions can be found with a slight change in the total commitment costs using various versions of our proposed method. The acceptable cost difference (about 2%) verifies that the approximation and sensitivity-based measure estimation with appropriately selected parameters introduce trivial impacts on the final commitment plan. The reducing computational complexity demonstrates the effectiveness of the proposed iterative method and the sensitivity-based approach.

VII. Conclusion

This paper presents a generation-side method to improve power system primary frequency response. We assign costs to FSD resources and formulate a minimum-cost PFR-constrained optimization problem for a smarter use of presently-available technology. The proposed iterative solution approach and sensitivity-based method prove to be effective for finding the near-optimal commitment of FSDs with significant reductions in computational complexity. The minimum commitment cost of FSD provides a basis to evaluate inertia services for power systems.

In this paper, we only focus on the controls of FSDs, but the proposed iterative algorithm to determine the minimum-cost deployment plan for FSDs is general enough to be applied for other types of sources that are capable to mimic inertia. The optimization problem presented in this paper is capable to be modified to consider stochastic processes or uncertainty in power system. Another potential application of the proposed methods is to formulate a PFR-constrained unit commitment problem that optimizes the commitment and operating points of both generation and demand resources. We will address those topics in future work.

VIII. Discussions on FSD Control Algorithms

The core idea of different existing FSD control algorithms [14], [20], [22], [34] is typically to provide droop control. In other words, those FSDs respond to the frequency deviation Δf - the change of frequency. The control algorithm proposed in this paper aims to change storage output, responding to $\Delta \dot{f}$ - the rate of change of frequency. Thus, we use droop control as a reference control algorithm, as shown in Fig. 21, for comparison purposes.

We note that the proposed iterative sensitivity-based algorithm in Section III-V is general enough to consider different FSD dynamic models under different control algorithms. Here, we use the IEEE 118-bus test system to illustrate the contribution of multi-site FSDs under different control algorithms. However, when we considered droop control for FSDs (constraint (3d) is modified to consider the range of D_{sp}), we could not find a solution to satisfy minimum frequency and maximum RoCoF magnitude requirements at the same time for all buses, no matter whether we were using the proposed iterative sensitivity-based algorithm or the generic method in Section III (searching in the solution space, extremely computationally burdensome but must find the optimal solution if any). The reason may be that the droop control has a limited capability to lower the RoCoF magnitude, which is mostly determined by inertia.

To verify our guess, we formulate and solve the FSD commitment problem, in consideration only of the minimum frequency constraints. All cost coefficients are set to 1. Mathematically, we are solving optimization problem (3a), subject to constraints (3b) and (3d), without (3c). We compute RoCoFs for comparison purposes. Simulated frequencies and RoCoFs with FSDs under the proposed control algorithm (original (3d)) and droop control (constraint (3d) is modified to indicate the range of D_{sp}) are presented in Fig. 22. Given that the multi-FSDs are controlled to help system satisfy the minimum frequency requirement at each bus, both cases have improvements in RoCoFs. However, FSDs with the proposed algorithm makes more contribution to RoCoFs. For example, the frequencies at different buses in Fig. 22(a) oscillate more significantly than those in Fig. 22(b). Bus frequencies in Fig. 22(a) drop more slowly than those in Fig. 22(b). Specifically, the maximum RoCoF magnitude in Fig. 22(a) is smaller than that in Fig. 22(b). This is because virtual inertial responses can slow down the change of frequency, and thus provide more time for system to pick up frequency.

Stabilizing frequency means not only to bring frequency back to the nominal value, but also to prevent frequency from changing too fast. As such, the advantage of the proposed control algorithm over the typical droop control is that it is able to significantly improve not only the minimum frequencies, but also the maximum RoCoF magnitudes.

IX. NOMENCLATURE FOR SECTIONS III AND IV

Superscript/Subscript

b	index of the buses with $b \in \mathcal{B} = \{1, 2, \ldots, B\}$
e	index of CEs with $e \in \mathcal{E} = \{1, 2, \ldots, E\}$
k	index of internal loops from 1 to K_s
m	index of metrics of interest with $m \in \mathcal{M} = \{f^{\min}, (-r)^{\max}\}$
M_b	index of requirements on metrics of interest with $M_b \in \{\underline{f}_b, -\bar{r}_b\}$
n	index of FSDs with $n \in \mathcal{N} = \{1, 2, \ldots, N\}$
s	index of outer loops from 1 to S
z	index from 0 to $\bar{Z}$ with $z \in \mathcal{Z}_n = \{0, 1, \ldots, \bar{Z}_n\}$
(s, k)	superscript for the inner step k of outer loop s

Variables/Parameters

$a^m_{b,e,n}\|_{\mathbf{H}}$	the linearised improvement of metric m by the introduction of FSD n virtual inertia during the z^{th} segment (from $h_{n,z-1}$ to $h_{n,z}$), as defined in (4a) [Hz/s or Hz/s^2]
$\tilde{a}^m_{b,e,n}\|_{\mathbf{H}}$	the approximation of $a^m_{b,e,n}\|_{\mathbf{H}}$, as defined in (9) [Hz/s or Hz/s^2]
c_n	objective function coefficient for virtual inertia
$\mathbf{c}$	vector $[c_1, c_2, \ldots, c_N]^T$
$d_{n,z}$	committed virtual inertia value of z^{th} segment for FSD n [s]
$\mathbf{d}$	vector $[\sum_{z=0}^{\bar{Z}_1} d_{1,z}, \sum_{z=0}^{\bar{Z}_2} d_{2,z}, \ldots, \sum_{z=0}^{\bar{Z}_N} d_{N,z}]$
$\mathbf{d}^{*(s,k)}$	optimal solution of optimization problem (5) at inner step k of outer loop s
E'	the number of contingency clusters
$f^{\min}_{b,e}\|_{\mathbf{x}}$	bus b minimum frequency after CE e, given the virtual inertia value setting $\mathbf{x}$ [Hz]
$\underline{f}_b$	bus b minimum frequency requirement [Hz]
$G^m_{b,e,n}\|_{\mathbf{H}^{(s)}}$	piece-wisely linearized $\frac{\partial m_{b,e}\|_{\mathbf{H}}}{\partial q^s_n}$
$h_{n,z}$	the z^{th} end point of the $\bar{Z}_n$-segmented range $[\underline{H}_n, \bar{H}_n]$ with $h_{n,-1} = 0$ [s]
$\Delta h_{n,z}$	$h_{n,z} - h_{n,z-1}$ as defined in (4c) [s]
$\mathbf{h}_n$	vector $[h_{n,0} = \underline{H}_n, h_{n,1}, \ldots, h_{n,\bar{Z}_n} = \bar{H}_n]^T$
h_n	FSD n current virtual inertia setting [s]
$\underline{H}_n, \bar{H}_n$	lower and upper bounds of x_n (h_n) [s]
$\underline{\mathbf{H}}$	vector $[\underline{H}_1, \underline{H}_2, \ldots, \underline{H}_N]^T$
$\bar{\mathbf{H}}$	vector $[\bar{H}_1, \bar{H}_2, \ldots, \bar{H}_N]^T$
$\mathbf{H}$	defined as $[h_1, h_2, \ldots, h_N]^T$
$\hat{\mathbf{H}}_{n,z}$	a mutation of $\mathbf{H} = [\ldots, h_n, \ldots]^T$ by changing FSD n virtual inertia setting from h_n to $h_{n,z}$
J	number ($= \bar{Z}_n + 2$) of possible virtual inertia values for each FSD
$m_{b,e}\|_{\mathbf{x}}$	bus b metric m value after CE e, given the virtual inertia value setting $\mathbf{x}$ [Hz] or [Hz/s]
p^s_n	real power output of FSD n
$\tilde{p}^s_n$	estimated p^s_n through the playback of the frequency measurements at each bus with the given virtual inertia value
q^s_n	reactive power output of FSD n
$\tilde{q}^s_n$	estimated q^s_n through the playback of the frequency measurements at each bus with the given virtual inertia value
$r^{\max}_{b,e}\|_{\mathbf{x}}$	bus b maximum RoCoF magnitude after CE e, given the virtual inertia value setting $\mathbf{x}$ [Hz/s]
$\bar{r}_b$	bus b maximum RoCoF magnitude requirement [Hz/s]
R	the number of buses where the N FSDs are installed
R'	the number of bus clusters where the N FSDs are installed
$S^m_{b,e,n}\|_{\mathbf{H}^{(s)}}$	piece-wisely linearized $\frac{\partial m_{b,e}\|_{\mathbf{H}}}{\partial p^s_n}$
t_0	the time when the CE e occurs
$t_{e,end}$	the time when the last bus in the system has reached its minimum frequency
T_e	number of sub-periods from t_0 to $t_{e,end}$
$u_{n,z}$	status variable of z^{th} segment for FSD n
$v^m_{b,e}\|_{\mathbf{H}}$	the minimum improvement needed such that each metric is within its limit as defined in (4b) [Hz/s or Hz/s^2]
x_n	virtual inertia value of each FSD [s]
$\mathbf{x}$	vector $[x_1, x_2, \ldots, x_N]^T$
$\bar{Z}_n$	number of segments within the range $[\underline{H}_n, \bar{H}_n]$
$\alpha^{(s)}_n$	the factor used to shrink solution space
$\beta^{m(s,k)}_{b,e}$	the factor used to strengthen requirements
η_β	the factor used to update $\beta^{(s)}_{b,e}$

REFERENCES

[1] W. Freitas, W. Xu, C. M. Affonso, and Z. Huang, "Comparative analysis between ROCOF and vector surge relays for distributed generation applications," *IEEE Trans. Power Del.*, vol. 20, no. 2, pp. 1315–1324, Apr. 2005.

[2] Electric Reliability Council of Texas, Inc., Future Ancillary Services in ERCOT, ERCOT Concept Paper, Nov. 2013. [Online]. Available: http://www.ercot.com/committees/other/fast/index.html

[3] "Frequency Response and Frequency Bias Setting," NERC Reliability Std. BAL-003–1, Feb. 2013.

[4] P.M. Anderson and M. Mirheydar, "A low-order system frequency response model," *IEEE Trans. Power Syst.*, vol. 5, no. 3, pp. 720–729, Aug. 1990.

[5] D. Hau Aik, "A general-order system frequency response model incorporating load shedding: Analytic modeling and applications," *IEEE Trans. Power Syst.*, vol. 21, no. 2, pp. 709–717, May 2006.

[6] E. Ela *et al.*, "Market designs for the primary frequency response ancillary service—Part I: Motivation and design," in *IEEE Trans. Power Syst.*, vol. 29, no. 1, pp. 421–431, Jan. 2014.

[7] H. Ahmadi and H. Ghasemi, "Security-constrained unit commitment with linearized system frequency limit constraints," *IEEE Trans. Power Syst.*, vol. 29, no. 4, pp. 1536–1545, Jul. 2014

[8] R. Bhana and T. Overbye, "The commitment of interruptible load to ensure adequate system primary frequency response," *IEEE Trans. Power Syst.*, vol. 31, no. 3, pp. 2055–2063, May 2016.

[9] T. Xu, W. Jang and T. Overbye, "An economic evaluation tool of inertia services for systems with integrated wind power and fast-acting storage resources," in *Proc. 49th Hawaii Int. Conf. Syst. Sci.*, Koloa, HI, USA, 2016, pp. 2456–2465.

[10] T. Xu, W. Jang and T. Overbye, "Application of set-theoretic method to assess the locational impacts of virtual inertia services on the primary frequency responses," in *Proc. IEEE Power Energy Conf. Illinois*, Urbana, IL, USA, 2016, pp. 1–6.

[11] A. D. Del Rosso and S. W. Eckroad, "Energy storage for relief of transmission congestion," *IEEE Trans. Smart Grid*, vol. 5, no. 2, pp. 1138–1146, Mar. 2014.

[12] D. Wu, C. Jin, P. Balducci and M. Kintner-Meyer, "An energy storage assessment: Using optimal control strategies to capture multiple services," in *Proc. IEEE Power Energy Soc. General Meeting*, Denver, CO, USA, 2015, pp. 1–5.

[13] K. Baker, G. Hug and X. Li, "Energy storage sizing taking into account forecast uncertainties and receding horizon operation," *IEEE Trans. Sustain. Energy*, vol. 8, no. 1, pp. 331–340, Jan. 2017.

[14] S. J. Lee *et al.*, "Coordinated control algorithm for distributed battery energy storage systems for mitigating voltage and frequency deviations," *IEEE Trans. Smart Grid*, vol. 7, no. 3, pp. 1713–1722, May 2016.

[15] ABB Group, "Energy storage and grid stabilization," 2016. [Online]. Available: http://www.abb.com/product/us/9aac167805.aspx

[16] Ecoult, "MW-Scale Regulation Services on the PJM Grid in Pennsylvania," 2017. [Online]. Available: http://www.ecoult.com/case-studies/case-study-examples/6-mw-scale-regulation-services-in-the-us-on-the-pjm-grid-in-pennsylvania

[17] California Energy Storage Alliance, "Energy storage—A cheaper, faster and cleaner alternative to conventional frequency regulation," 2016. [Online]. Available: https://www.ice-energy.com/wp-content/uploads/2016/04/cesa_energy_storage_for_frequency_regulation.pdf

[18] N. W. Miller, K. Clark and M. Shao, "Frequency responsive wind plant controls: Impacts on grid performance," in *Proc. IEEE Power Energy Soc. General Meeting*, San Diego, CA, USA, 2011, pp. 1–8.

[19] S. Riffat and X. Ma, "Thermoelectrics: A review of present and potential applications," *Appl. Thermal Eng.*, vol. 23, no. 8, pp. 913–935, 2003.

[20] G. Delille, B. Francois and G. Malarange, "Dynamic frequency control support by energy storage to reduce the impact of wind and solar generation on isolated power system's inertia," *IEEE Trans. Sustain. Energy*, vol. 3, no. 4, pp. 931–939, Oct. 2012.

[21] M. H. Wang, "Application of flywheel energy storage system to enhance transient stability of power systems," *Electr. Power Compon. Syst.*, vol. 33, no. 4, pp. 463–479, 2005.

[22] A. Ortega and F. Milano, "Generalized model of VSC-based energy storage systems for transient stability analysis," *IEEE Trans. Power Syst.*, vol. 31, no. 5, pp. 3369–3380, Sep. 2016.

[23] B. C. Pal *et al.*, "A linear matrix inequality approach to robust damping control design in power systems with superconducting magnetic energy storage device," *IEEE Trans. Power Syst.*, vol. 15, no. 1, pp. 356–362, Feb. 2000.

[24] P. Kundur, *Power System Stability and Control*. New York, NY, USA: McGraw-Hill, 1994.

[25] A. Wood *et al.*, *Power Generation, Operation and Control*, 3rd ed. Hoboken, NJ, USA: Wiley, 2013.

[26] T. Xu and N. Zhang, "Coordinated operation of concentrated solar power and wind resources for the provision of energy and reserve services," *IEEE Trans. Power Syst.*, vol. 32, no. 2, pp. 1260–1271, Mar. 2017.

[27] PPA Energy, "Rate of Change of Frequency (ROCOF), Review of TSO and Generator Submissions," Final Report, May. 2013. [Online]. Available: http://www.cer.ie/docs/000260/cer13143-(a)-ppa-tnei-rocof-final-report.pdf

[28] Power flow cases, 2017. [Online]. Available: http://publish.illinois.edu/smartergrid/power-cases/

[29] R. Christie, "Power systems test case archive," Univ. Washington, Seattle, WA, USA, 1998. [Online]. Available: http://www.ee.washington.edu/research/pstca/.

[30] S. Dutta and T. J. Overbye, "Feature extraction and visualization of power system transient stability results," *IEEE Trans. Power Syst.*, vol. 29, no. 2, pp. 966–973, Mar. 2014.

[31] T. Xu and T. Overbye, "Real-time event detection and feature extraction using PMU measurement data", in *Proc. IEEE Int. Conf. Smart Grid Commun.*, Miami, FL, USA, 2015, pp. 265–270.

[32] PowerWorld, 2017. [Online]. Available: http://www.powerworld.com/

[33] A. A. Akhil *et al.*, "DOE/EPRI electricity storage handbook in collaboration with NRECA," Feb. 2015. [Online]. Available: http://www.sandia.gov/ess/publications/SAND2015–1002.pdf

[34] K. Vu, R. Masiello and R. Fioravanti, "Benefits of fast-response storage devices for system regulation in ISO markets," in *Proc. 2009 IEEE Power Energy Soc. General Meeting*, Calgary, AB, Canada, 2009, pp. 1–8.

Ti Xu (S'12) received the B.S. degree from Tsinghua University, Beijing, P.R.C., in 2011, and the M.S. and Ph.D. degrees from the University of Illinois at Urbana-Champaign, Urbana, IL, USA, in 2014 and 2017, respectively. He is currently a Postdoctoral Researcher at the Department of Electrical and Computer Engineering, Texas A&M University, College Station, TX, USA.

Wonhyeok Jang (S'10) received the B.S. and M.S. degrees in electrical engineering from Sungkyunkwan University, Seoul, Korea, and the Ph.D. degree from the University of Illinois at Urbana-Champaign, Urbana, IL, USA, in 2017. He is currently a Postdoctoral Researcher at the Department of Electrical and Computer Engineering, Texas A&M University, College Station, TX, USA.

Thomas J. Overbye (S'87–M'92–SM'96–F'05) received the B.S., M.S., and Ph.D. degrees in electrical engineering from the University of Wisconsin-Madison, Madison, WI, USA. He is currently a Professor of Electrical and Computer Engineering at the Texas A&M University, College Station, TX, USA.